FEBRUARY 10 2026

Impact of building wake turbulence on the noise footprint of a dipole source

Jatinder Goyal ; Frits de Prenter ; Daniele Ragni ; Damiano Casalino

J. Acoust. Soc. Am. 159, 1304–1315 (2026)
https://doi.org/10.1121/10.0042402

JASA ARTICLE

Impact of building wake turbulence on the noise footprint of a dipole source

Jatinder Goyal,[1,2,a] Frits de Prenter,[1,b] Daniele Ragni,[1,c] and Damiano Casalino[1,3,d]
[1]*Department of Flow Physics and Technology, Faculty of Aerospace Engineering, Delft University of Technology, Delft, The Netherlands*
[2]*Suzlon Energy Limited, Hengelo, The Netherlands*
[3]*Dassault Systemes Deutschland GmbH, Stuttgart, Germany*

ABSTRACT:
Building-generated turbulence can significantly influence the propagation of noise from advanced air mobility (AAM) vehicles operating in urban environments, yet its impact on acoustic variability remains poorly quantified. In this study, the effect of an isolated building wake on sound propagation is investigated using time-resolved Lattice-Boltzmann very-large-eddy simulations. A simplified tonal acoustic source representative of an AAM vehicle is placed downstream of the building, and the resulting unsteady sound field is analyzed within and downstream of the turbulent wake. The results show that wake-induced turbulence produces pronounced temporal fluctuations in the received sound pressure level, with variability exceeding 3 dB in localized regions. These fluctuations extend beyond the physical extent of the wake due to interference effects and reflected propagation paths from the building and ground. Analysis along selected propagation directions indicates a strong correlation between turbulence-induced velocity fluctuations and acoustic variability along direct propagation paths, while this correlation weakens in regions dominated by multiple reflections. The findings emphasize the importance of accounting for unsteady, building-induced flow effects when evaluating AAM noise in urban environments.
https://doi.org/10.1121/10.0042402
(Received 15 August 2025; revised 16 January 2026; accepted 18 January 2026; published online 10 February 2026)
[Editor: Michael J. White] Pages: 1304–1315

NOMENCLATURE

H	building height, m
L	length of ray path, m
p	static pressure, Pa
p_{ref}	reference sound pressure, 2×10^{-5} Pa
$p_{\text{rms, source}}$	Average p_{rms} over a sphere of 1 m radius around the acoustic source, Pa
p_{rms}	root-mean-square (RMS) of acoustic pressure fluctuations over a given time window or frequency band, Pa
S	symmetric part of the velocity gradient tensor, $\frac{1}{2}(\nabla\vec{U} + (\nabla\vec{U})^T)$, 1/s
t	time, s
$\vec{U}$	velocity vector, m/s
U_x	streamwise velocity component, m/s
$u_\star$	friction velocity, m/s
X	streamwise coordinate, m
Y	vertical coordinate, m
Y_0	roughness length, m
Z	spanwise coordinate, m
PSD	power spectrum density, dB/Hz
SPL	sound pressure level, $20\log_{10}\left(\frac{p_{\text{rms}}}{p_{\text{ref}}}\right)$, dB
$\bar{\sigma}_{\lvert\vec{U}\rvert,\text{norm}}$	Velocity fluctuations, $\sqrt{\frac{1}{L}\int_0^L \left(\frac{\sigma(\lvert\vec{U}\rvert)(l)}{\sigma(\lvert\vec{U}\rvert)_{\max}}\right)^2 dl}$
$\bar{\sigma}_{p,\text{norm}}$	Acoustic variability, $\sqrt{\frac{1}{L}\int_0^L \left(\frac{\sigma(p_{\text{rms}})(l)\cdot l}{p_{\text{rms, source}}}\right)^2 dl}$
κ	Von Karman constant
λ_2	second largest eigenvalue of the symmetric tensor $(S^2 + \Omega^2)$, used for vortex identification
Ω	antisymmetric part of the velocity gradient tensor, $\frac{1}{2}(\nabla\vec{U} - (\nabla\vec{U})^T)$, 1/s
σ	standard deviation

I. INTRODUCTION

Ground-based transportation in dense urban areas is increasingly constrained by congestion and limited infrastructure. A promising alternative is to exploit the third dimension: air transportation, which can provide faster, more flexible, and on-demand mobility within and between cities. Advanced air mobility (AAM) embodies this vision, focusing on innovative aerial vehicles, such as electric vertical takeoff and landing (eVTOL) aircraft, designed for urban and semi-urban environments. Examples include aircraft developed by Joby Aviation, Inc. (Santa Cruz, CA), Archer Aviation Inc. (San Jose, CA), Volocopter GmbH (Bruchsal, Germany), EHang Holdings

[a]Email: j.goyal@tudelft.nl
[b]Electronic mail: f.deprenter@tudelft.nl
[c]Electronic mail: d.ragni@tudelft.nl
[d]Electronic mail: d.casalino@tudelft.nl

https://doi.org/10.1121/10.0042402

Limited (Guangzhou, China), and Wisk Aero LLC (Mountain View, CA). The feasibility of AAM is steadily increasing due to advances in battery technology and electric propulsion, which enable distributed propulsion architectures that exploit propeller–airframe interactions to partially offset the low energy density of batteries.[1] AAM concepts are expected to support a wide range of applications, including alleviating traffic congestion, enhancing emergency response, enabling faster intra- and inter-city travel, improving cargo logistics, and facilitating infrastructure inspection.[2]

Many proposed AAM vehicle designs employ multiple propellers distributed along the airframe and are expected to operate at relatively low altitudes compared to conventional commercial aviation, with takeoff and landing infrastructure, referred to as vertiports, situated within dense urban environments.[3] However, the combination of low-altitude operation, distributed propulsion systems, and close proximity to the built environment raises significant concerns regarding community noise impact, which remains a key barrier to the widespread public acceptance of AAM vehicles.[4–6]

A substantial body of existing research has focused on characterizing AAM noise at the source level, including tonal and broadband contributions from propellers.[7–9] In parallel, prior work in outdoor and urban acoustics has extensively documented sound propagation in built environments, including multipath interference and reverberation effects.[10] In addition, turbulence-induced sound fluctuations have been investigated from both theoretical and experimental perspectives, often considering homogeneous or externally prescribed turbulence fields.[11–13]

Separately, the generation of turbulence by buildings and urban structures is a well-established topic in wind engineering and urban fluid mechanics. It is widely recognized that building-induced turbulence is highly inhomogeneous, anisotropic, and dominated by large coherent structures, such as separation bubbles, shear layers, horseshoe vortices, and wake meandering.[14–16] These flow features arise directly from the interaction between the mean wind and the built geometry and differ fundamentally from the homogeneous or equilibrium turbulence typically assumed in canonical atmospheric or aeroacoustic studies.

In realistic urban environments, AAM vehicles are therefore expected to operate within such unsteady, building-generated flowfields, particularly during takeoff and landing. In these conditions, the sound received by a ground observer results from the superposition of direct and reflected acoustic paths, each traversing regions of spatially and temporally varying flow velocity. Large-scale turbulent structures in building wakes can locally modify acoustic propagation times and ray trajectories, leading to time-dependent phase variations between propagation paths. Even for a stationary acoustic source, these effects can produce alternating constructive and destructive interference at the observer, resulting in significant temporal modulation of the received sound level. Time-resolved coupling of unsteady flow and acoustic propagation is, therefore, required to capture temporal variability in interference patterns and reflected propagation paths; such effects cannot be represented using steady or frozen-flow acoustic models.

While the individual roles of urban turbulence, multipath propagation, and turbulence-induced sound variability have been addressed in prior work, they are often treated in isolation or using prescribed turbulence fields. In particular, turbulence is commonly modeled as homogeneous, isotropic, or externally imposed along the propagation path. The explicit, time-resolved interaction between building-generated, spatially inhomogeneous turbulence and acoustic wave propagation has received comparatively limited attention, primarily due to the high computational cost associated with resolving both unsteady flowfields and acoustics simultaneously. The present study addresses this gap by explicitly resolving the coupled, time-dependent interaction between building-generated turbulence and sound propagation.

To isolate propagation effects from source-level modulation, the acoustic source is intentionally simplified and modeled as a compact dipole oscillating vertically at a fixed frequency of 100 Hz. This frequency is representative of dominant tonal components or harmonics generated by several AAM vehicles, including Vertical Aerospace's VX4 (Vertical Aerospace Group Ltd., Bristol, UK),[17] CityAirbus (Airbus Helicopters, Donauwörth, Germany),[18] NASA's X-57 Maxwell (NASA, Edwards, CA),[19] and the second harmonic of Joby Aviation propeller tones.[20–22] By maintaining a fixed and idealized source, the present study isolates propagation-induced variability from source-level modulation, allowing the effects of building-generated turbulence on sound propagation to be examined directly.

The paper begins by describing the computational setup and flowfield validation, followed by an analysis of instantaneous flow and acoustic fields. A statistical characterization of acoustic variability is then presented, linking observed sound-level fluctuations to turbulence encountered along acoustic propagation paths. The findings aim to support the development of improved noise assessment methodologies for AAM operations in complex urban environments.

II. METHODOLOGY

The present study employs lattice-Boltzmann very-large-eddy simulations (LB-VLES) performed with SIMULIA PowerFLOW 6–2021-R6 (Dassault Systèmes SIMULIA, Johnston, RI). This approach has been extensively validated for AAM aeroacoustics at both rotor[23–27] and full-vehicle scales[28,29] in the past. The inherently low numerical dissipation and dispersion of the lattice-Boltzmann (LB) method[30,31] make it particularly well-suited for capturing the propagation of acoustic waves over large distances.

The very-large-eddy simulation (VLES) is a hybrid turbulence model. Depending on the local values of the flow shear stresses and other local properties of the flow, the relaxation time of the LB collision operator is dynamically adjusted from the value corresponding to an isotropic homogeneous turbulence field computed using a renormalization-group k-ϵ formulation,[32] and a value corresponding to the slow motion of the resolved turbulent structures,[33] with the modeled contribution diminishing as the turbulent structures become increasingly

resolved. A detailed description of the underlying LB scheme can be found in Succi[34] and Shan *et al.*[35]

The current section first describes the computational domain and coordinate system, followed by the building geometry and inflow conditions. The acoustic source specification and boundary conditions are then presented, and the section concludes with the simulation strategy and associated computational cost.

A. Computational domain and coordinate system

The computational domain (Fig. 1) extends 1400 m ($28H$) in the streamwise direction, 1000 m ($20H$) vertically, and 900 m ($18H$) in the spanwise direction, where $H = 50$ m is the building height. The domain is divided into seven variable-resolution (VR) regions, with the cell volume increasing by a factor of eight between successive regions. The finest resolution region (VR7) is centered around the dipole source [Fig. 1(c)] and extends up to five acoustic wavelengths in all directions. This region lies within the primary region of interest, VR6, which measures $400 \times 150 \times 50$ m^3 [Fig. 1(c)]. All analyses presented in this paper are conducted within the VR6 region. The coarser outer regions act as buffer zones, keeping the far-field boundaries sufficiently distant and minimizing spurious reflections to ensure undisturbed acoustic propagation within the region of interest.

B. Building geometry and inflow conditions

The building represents a mid-rise urban structure inspired by the TU Delft Aerospace Faculty building.[36,37] Its dimensions are 50 m (H) height, 10 m ($0.2H$) streamwise, and 20 m ($0.4H$) depth. The upstream face is located 200 m downstream of the inlet to allow sufficient flow development [see Fig. 1(c)].

A logarithmic atmospheric boundary layer profile typical of urban areas is prescribed at the inlet:[38]

$$U_x(Y) = \frac{u_\star}{\kappa} \log_{10}\left(\frac{Y}{Y_0} + 1\right), \tag{1}$$

with friction velocity $u_\star = 1.23$ m/s, von Kármán constant $\kappa = 0.41$, and roughness length $Y_0 = 0.1$ m. This yields mean wind speeds of ≈ 8 m/s at rooftop height ($Y = H$) and ≈ 9 m/s at $Y = 2H$. Only the mean wind profile is imposed at the inlet; no synthetic turbulence is introduced, as the study focuses on turbulence generated by the building wake rather than upstream inflow fluctuations.

C. Acoustic source definition

The noise source is modeled as a 0.5 m cube located 100 m downstream of the building's front face and 100 m above the ground [i.e., 50 m above the roof, Fig. 1(c)]. The

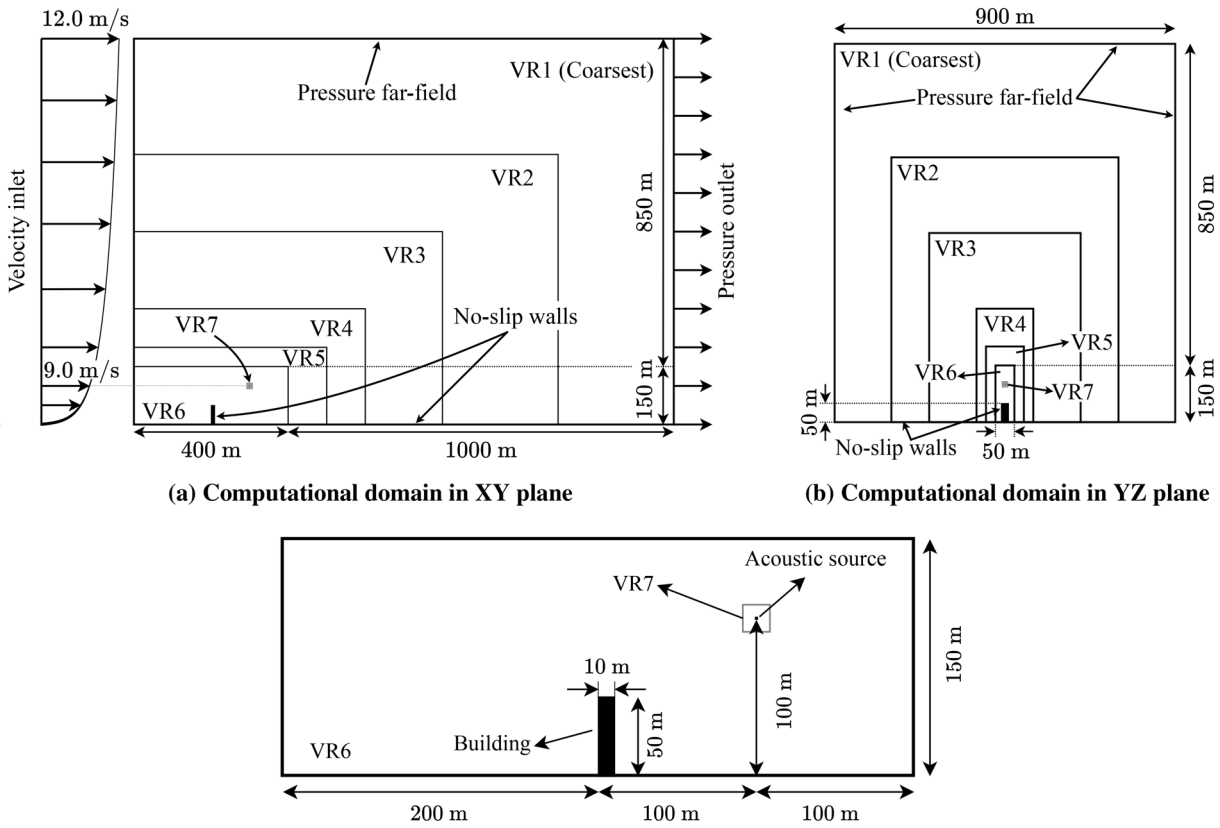

(a) Computational domain in XY plane

(b) Computational domain in YZ plane

(c) Primary region of interest (VR6)

FIG. 1. Overview of the computational domain and region of interest. (Note: X is streamwise, Y vertical, and Z spanwise; this differs from the convention commonly used in wind engineering where Z is vertical).

https://doi.org/10.1121/10.0042402

horizontal faces of the cube are assigned a sinusoidal wall-normal velocity of amplitude 2 m/s at 100 Hz, mimicking a compact dipole typical of AAM rotor noise.[17–22] The resulting source generates a root-mean-square (RMS) pressure of 17.3 Pa averaged over a 1 m radius sphere. The simplified source representation is intentionally adopted to isolate propagation effects from source-induced modulation.

D. Boundary conditions and additional physics

The ground and building surfaces are treated using a pressure-gradient extended wall model,[39,40] in which wall shear stresses are imposed through a generalized law-of-the-wall formulation[41] without resolving the viscous sublayer. Acoustically, these surfaces act as rigid reflectors with specular reflection. Pressure outlet conditions are applied at the domain exit, and pressure far-field conditions on all lateral and top boundaries.

The air temperature is assumed to be uniform throughout the domain, resulting in a constant speed of sound with height. Over the 150 m vertical extent of the region of interest (VR6), the standard atmospheric lapse rate would induce a temperature drop of less than 1 K and a sound–speed variation of $\approx$0.6 m/s, producing negligible refraction effects on the scales investigated here.

In LB-VLES, air absorption arises naturally through viscous and bulk damping associated with the relaxation process during the collision step of the LB method. This mechanism introduces physical attenuation of acoustic waves, although molecular relaxation effects (e.g., humidity-dependent absorption) are not explicitly modeled. However, for the given source frequency and the maximum propagation distances considered within VR6, the expected attenuation is less than 0.05 dB, making its effect negligible on the reported results.

The vortex shedding frequency of the building, estimated using a characteristic depth of 20 m and accounting for the vertical wind-speed gradient, spans approximately 0.005–0.08 Hz, corresponding to local flow velocities ranging from 1 m/s near the ground to 8 m/s at rooftop level and assuming a Strouhal number in the range 0.1–0.2.[42] These characteristic frequencies are 3 orders of magnitude lower than the acoustic source frequency of 100 Hz, ensuring a clear separation between hydrodynamic and acoustic time scales.

E. Simulation strategy and computational cost

As the vortex shedding frequency is significantly lower than the acoustic frequency, extended simulation times are required to resolve the turbulent wake. However, high-resolution acoustic simulations require approximately 20 voxels per wavelength (voxel size of 0.17 m for 100 Hz at 343 m/s), making long-duration runs computationally prohibitive. To address this, a two-stage simulation strategy is adopted.

(1) A coarse-resolution simulation with a finest voxel size of 0.5 m near the source is run for 1000 s, covering at least five full shedding cycles (based on a lower limit of 0.005 Hz). The first three cycles (approximately 625 s) are treated as a transient phase, while the remaining two cycles (375 s) are analyzed to confirm that the wake dynamics are adequately captured.
(2) The flowfield from the coarse simulation is then used to initialize a fine-resolution simulation with a finest voxel size of 0.086 m near the source. This high-resolution simulation is run for a total of 70 s, of which the initial 30 s are treated as a transient and excluded from post-processing. The remaining 40 s are used for acoustic analysis to investigate the interaction between unsteady wake dynamics and sound propagation.

This approach allows the unsteady flowfield and acoustic response to be captured consistently, while keeping the overall computational cost manageable.

Table I summarizes the grid specifications, time step, number of cells, and computational cost for both the coarse and fine simulations. The coarse simulation comprises approximately 1.9×10^6 equivalent fine cells, while the fine-resolution simulation contains approximately 3.6×10^8 equivalent fine cells. The coarse simulation, while relatively inexpensive, provides sufficient resolution to capture the wake dynamics for up to approximately 0.8 Hz (based on a convective velocity of 8 m/s at rooftop height), whereas the fine simulation, required for noise propagation, incurs a significantly higher computational cost.

A separate fine-resolution simulation without convection is also performed to serve as a reference. This simulation focused exclusively on the 100 Hz source and its harmonics, without incorporating any background flow or building wake effects. As a result, it did not require coarse initialization or long-duration runs. This simulation was executed for 10 s, with the first 5 s treated as transient and the remaining 5 s used for acoustic analysis.

III. RESULTS

Following the two-stage methodology described previously, the coarse-resolution simulation is first analyzed to verify that the dominant wake dynamics relevant to the

TABLE I. Grid specifications and computational cost for coarse and fine simulations.

Simulation	Simulation duration (s)	Finest voxel size (m)	Time step (s)	No. of equivalent fine cells	Average central processing unit (CPU) hours per second (hrs)	Total CPU hours for full run (hrs)
Coarse	1000	0.500	8.019×10^{-4}	18 66 268	2.4	2 400
Fine	70	0.086	1.376×10^{-4}	358 459 777	1634.0	1 14 380

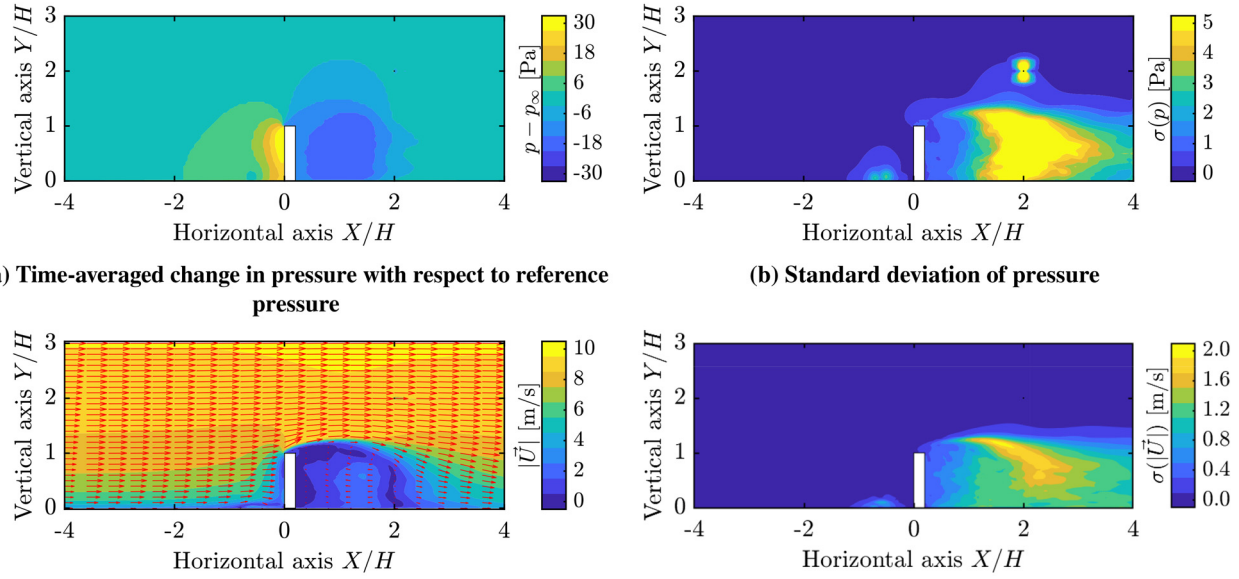

(a) Time-averaged change in pressure with respect to reference pressure

(b) Standard deviation of pressure

(c) Time-averaged velocity magnitude along with velocity vectors

(d) Standard deviation of velocity magnitude

FIG. 2. Time-average and standard deviation of flowfield over 375 s at $\boldsymbol{Z/H = 0}$ (coarse simulation).

present study are captured. Specifically, time-averaged and standard deviation fields of pressure and velocity magnitude are examined in the central plane ($Z/H = 0$). A frequency analysis of the velocity magnitude at multiple locations is also performed to confirm that the characteristic vortex shedding of the building is resolved. Based on this validation, the fine-resolution simulations are then used to assess the influence of temporal flow variations on the received acoustic signal over a 40 s post-transient period in the same plane.

A. Time-averaged flowfield (coarse simulation)

Figure 2 shows the time-averaged contours of pressure, velocity magnitude on the left, and their standard deviation on the right in the $Z/H = 0$ plane. The pressure field shown in Fig. 2(a) is plotted relative to the reference pressure. As expected, it shows a high-pressure region upstream and a low-pressure region in the wake. The region of significant pressure change with respect to the reference value is largely confined to approximately $1H$ upstream and $2H$ downstream of the building.

The standard deviation of pressure [Fig. 2(b)] reveals two distinct contributions: a localized figure-eight pattern centered around the dipole source (characteristic of an acoustic dipole) and broader fluctuations attributable to turbulence induced by the building. Due to the limited resolution of the coarse simulation, the 100 Hz acoustic wave is not fully resolved, and the dipole pattern remains confined to a small region near the source. Additionally, a horseshoe vortex forms upstream, leading to a localized area of elevated pressure fluctuations near the ground, consistent with prior studies.[43,44] In the wake region, pressure fluctuations arise primarily from unsteady vortex shedding and wake meandering.

Figures 2(c) and 2(d) show the time-averaged velocity magnitude and its standard deviation, respectively. In Fig. 2(c), velocity vectors are overlaid on the contours to indicate the flow direction. The velocity magnitude increases with height, consistent with the logarithmic wind profile imposed at the inlet. Near the ground, upstream of the building, the horseshoe vortex is evident, characterized by near-zero velocity and reversed flow,[43,44] in agreement with the pressure field in Fig. 2(a). A large recirculation zone forms downstream of the building, characterized by low velocity magnitudes and reversed flow.

The standard deviation of velocity magnitude [Fig. 2(d)] exhibits trends similar to those observed in the standard deviation of pressure. Elevated velocity fluctuations appear upstream in the horseshoe vortex region, as expected. In the wake region, the highest fluctuations occur along the edges of the recirculation zone, reflecting temporal variations in its extent and structure due to unsteady wake dynamics.

B. Velocity fluctuations (coarse simulation)

To further verify that the wake dynamics are adequately captured in the coarse simulations, the current section presents velocity fluctuation data and corresponding power spectral density (PSD) analyses at selected points in the building wake. The PSD was estimated from the velocity time series using Welch's averaged periodogram method applied to the 375 s analysis window of the coarse simulation. The mean was removed prior to spectral analysis. A Hanning window with 50% overlap was applied to reduce spectral leakage and variance. The fast Fourier transform (FFT) length was selected to achieve an effective frequency resolution of 0.005 Hz.

Velocity fluctuations are analyzed at three streamwise locations: (1) $X/H = 0.3$, (2) $X/H = 2.0$, and (3) $X/H = 3.0$,

https://doi.org/10.1121/10.0042402

all situated downstream of the building at a vertical position of $Y/H = 1.0$ and $Z/H = 0.0$ (see Fig. 3). The top row presents the time history of velocity magnitude fluctuations. The middle row shows the PSD on a linear scale to facilitate identification of dominant frequencies and associated Strouhal numbers, and the bottom row presents the PSD on a log–log scale to assess inertial-range behavior and spectral decay.

At all three locations [Figs. 3(a)–3(c)], the velocity fluctuations remain centered around zero with no discernible drift, indicating that the building wake is statistically stationary over the sampling interval.

At $X/H = 0.3$, velocity fluctuations range approximately between -0.5 and $+1.5$ m/s [Fig. 3(a)]. The corresponding spectrum [Fig. 3(e)] exhibits a dominant low-frequency peak at approximately 0.008 Hz. This low-frequency peak is attributed to a large-scale global wake mode, commonly described as wake meandering or shear-layer flapping, which originates from the separated flow at the building's roof edge. At this near-wake location, spectral components associated with classical bluff-body vortex shedding are not clearly observed. The log–log PSD [Fig. 3(g)] exhibits an approximately $-5/3$ spectral decay[45] over the limited frequency range 0.04–0.3 Hz, consistent with inertial-range–like behavior prior to the onset of numerical dissipation.

At $X/H = 2.0$, the velocity fluctuations intensify, spanning roughly from -4 to $+6$ m/s [Fig. 3(b)]. This location lies further within the developed wake region, where both large-scale wake meandering and classical bluff-body vortex shedding contribute significantly to the flow dynamics. The corresponding PSD [Fig. 3(e)] shows a dominant peak at approximately 0.005 Hz, together with a secondary peak at 0.048 Hz. The latter corresponds to a Strouhal number of approximately 0.12, consistent with classical vortex shedding from bluff bodies. The appearance of higher harmonics at this location reflects increased wake complexity and nonlinear interactions. The log–log PSD [Fig. 3(h)] exhibits an approximately $-5/3$ spectral decay over the frequency

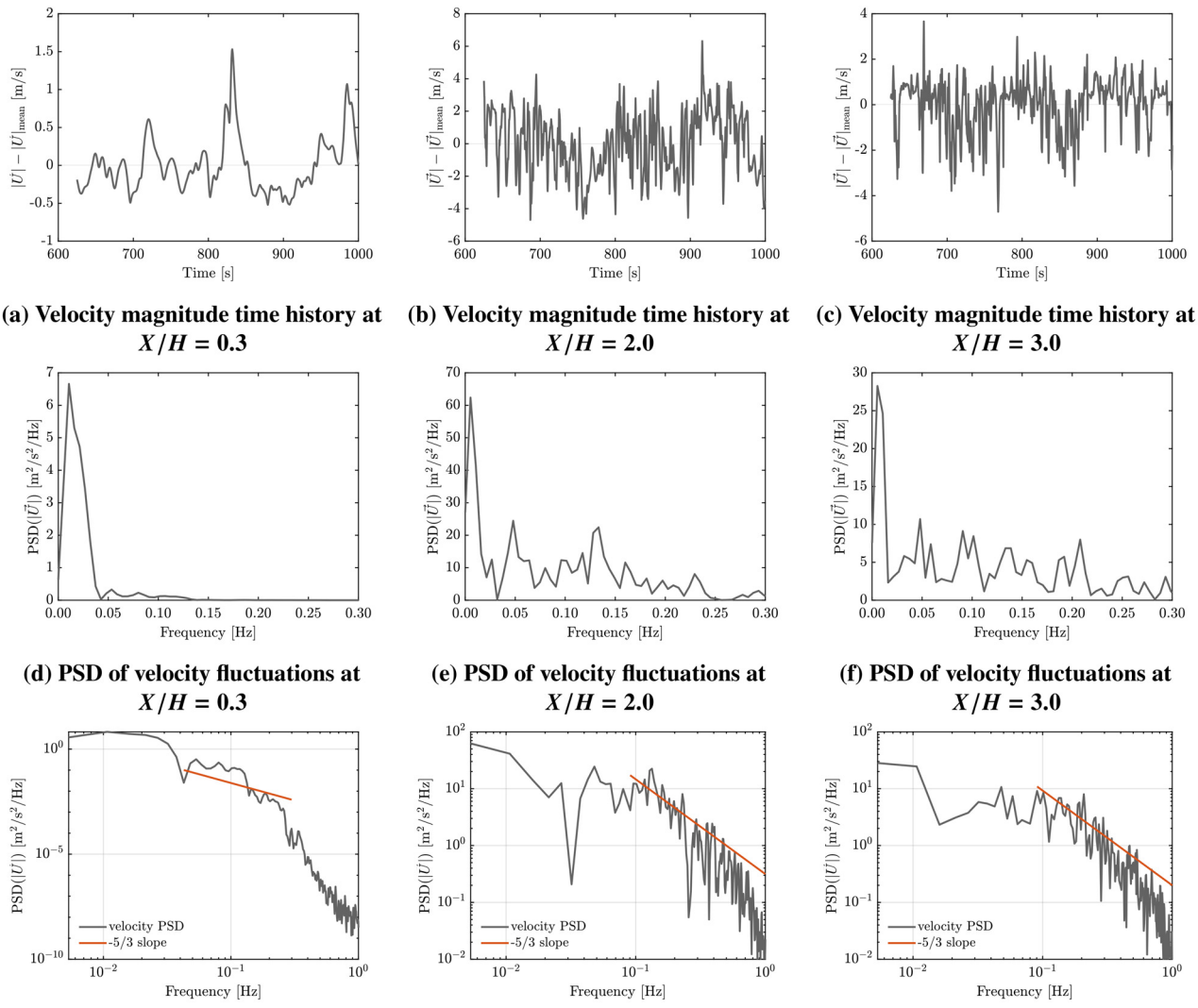

(a) Velocity magnitude time history at $X/H = 0.3$ **(b) Velocity magnitude time history at $X/H = 2.0$** **(c) Velocity magnitude time history at $X/H = 3.0$**

(d) PSD of velocity fluctuations at $X/H = 0.3$ **(e) PSD of velocity fluctuations at $X/H = 2.0$** **(f) PSD of velocity fluctuations at $X/H = 3.0$**

(g) Log–log PSD of velocity fluctuations at $X/H = 0.3$ **(h) Log–log PSD of velocity fluctuations at $X/H = 2.0$** **(i) Log–log PSD of velocity fluctuations at $X/H = 3.0$**

FIG. 3. Time history and PSD of velocity fluctuations at multiple streamwise positions in the building wake at $Y/H = 1.0, Z/H = 0.0$ (coarse simulation).

range 0.1–0.8 Hz, consistent with the upper frequency limit imposed by the coarse mesh resolution.

Further downstream, at $X/H = 3.0$, strong velocity fluctuations persist [Fig. 3(c)]. The corresponding PSD [Fig. 3(f)] retains dominant peaks within the previously identified low- and intermediate-frequency bands, with additional spectral energy distributed toward higher frequencies. The log–log PSD [Fig. 3(i)] continues to exhibit an approximately $-5/3$ spectral decay over 0.1–0.8 Hz, consistent with the limitations of the coarse mesh resolution.

Given the anisotropic nature of the building wake, the presence of mean shear, and the coarse spatial resolution of the VLES, the observed decay, which is similar to $-5/3$ decay, should be interpreted as a qualitative consistency check on spectral behavior rather than evidence of a fully developed inertial range.

These results demonstrate that the dominant frequencies in the velocity fluctuations are consistent with the Strouhal-number–based predictions in Sec. II D, indicating that the coarse-resolution simulation captures the primary wake dynamics relevant to the present study. Based on this validation, the subsequent fine-resolution simulation is assumed to provide a consistent representation of the wake and is therefore used for acoustic analysis over the 40 s post-transient period.

C. Instantaneous flowfield and sound pressure level (SPL) (fine simulation)

This section presents snapshots of the instantaneous flowfield from the fine-resolution simulations to illustrate the spatial and temporal variability of the building wake and its impact on the acoustic footprint. The analysis begins with λ_2 flow structure visualizations, where λ_2 vortex criterion is a vortex core line detection algorithm that can adequately identify vortices from a three-dimensional fluid velocity field,[46] followed by streamwise velocity contours at two time instances, and concludes with corresponding SPL fields, compared against the no-convection case.

Figure 4 shows the instantaneous flow structures visualized using the λ_2 criterion ($\lambda_2 = -1$), overlaid with contours of streamwise velocity. The key features, such as the upstream horseshoe vortex and wake meandering in both vertical and spanwise directions, are clearly evident.

To highlight the temporal unsteadiness, streamwise velocity contours in the mid-span plane ($Z/H = 0$) at two representative time instances are shown in Figs. 5(a) and 5(b), with their difference plotted in Fig. 5(c). While the velocity field remains relatively unchanged outside the wake, substantial differences are observed within the wake region, highlighting the unsteady nature of the flow.

The corresponding SPL fields at the same two time instances are shown in Fig. 6. For comparison, SPL fields from the no-convection case at two different times are also included. The SPL was computed by bandpassing the pressure signal between 95 and 105 Hz over a 0.2 s window centered around each time instant. Temporal changes in SPL are quantified via the difference computed directly in the decibel (dB) scale. As shown in Eq. (2), the direct difference in decibels simplifies interpretation, as it directly corresponds to the logarithmic ratio of the respective p_{rms} values,

$$\Delta\mathrm{SPL} = \mathrm{SPL}_2 - \mathrm{SPL}_1 = 20\log_{10}\left(\frac{p_{\mathrm{rms}_2}}{p_{\mathrm{rms}_1}}\right). \tag{2}$$

For the no-convection case, SPL fields at different time instances [Figs. 6(a) and 6(b)] are nearly identical, indicating a steady acoustic environment. A dipole pattern centered around the source is visible, with interference fringes downstream of the building and near the ground due to reflections. Additional fringes are seen upstream and above the building, due to reflections and diffraction from the building's top edges. The SPL difference field [Fig. 6(c)] confirms temporal stability, showing negligible differences across most of the domain. Isolated spikes appearing in regions with very low p_{rms} are attributed to the numerical amplification of small changes in near-zero p_{rms} values, as explained by Eq. (2).

In contrast, the convection case exhibits clear temporal variability. The SPL fields at the representative time

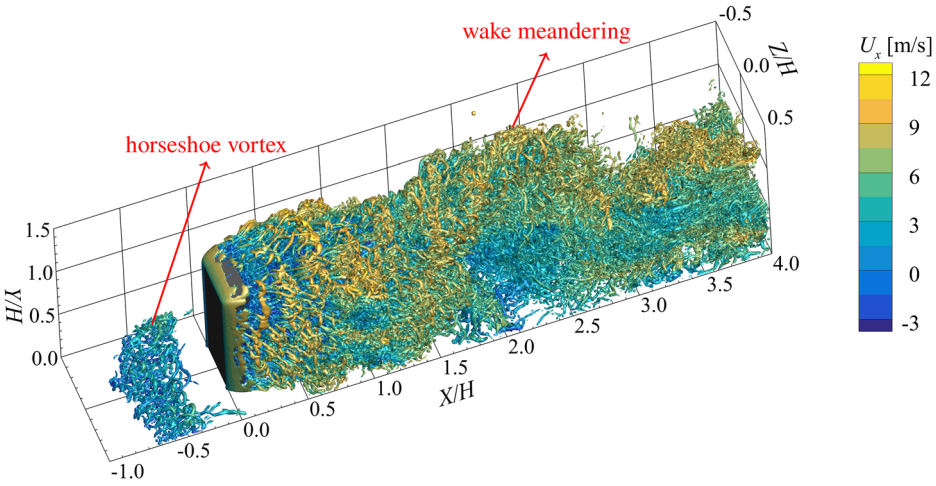

FIG. 4. λ_2 visualization of the instantaneous wake (fine simulation).

https://doi.org/10.1121/10.0042402

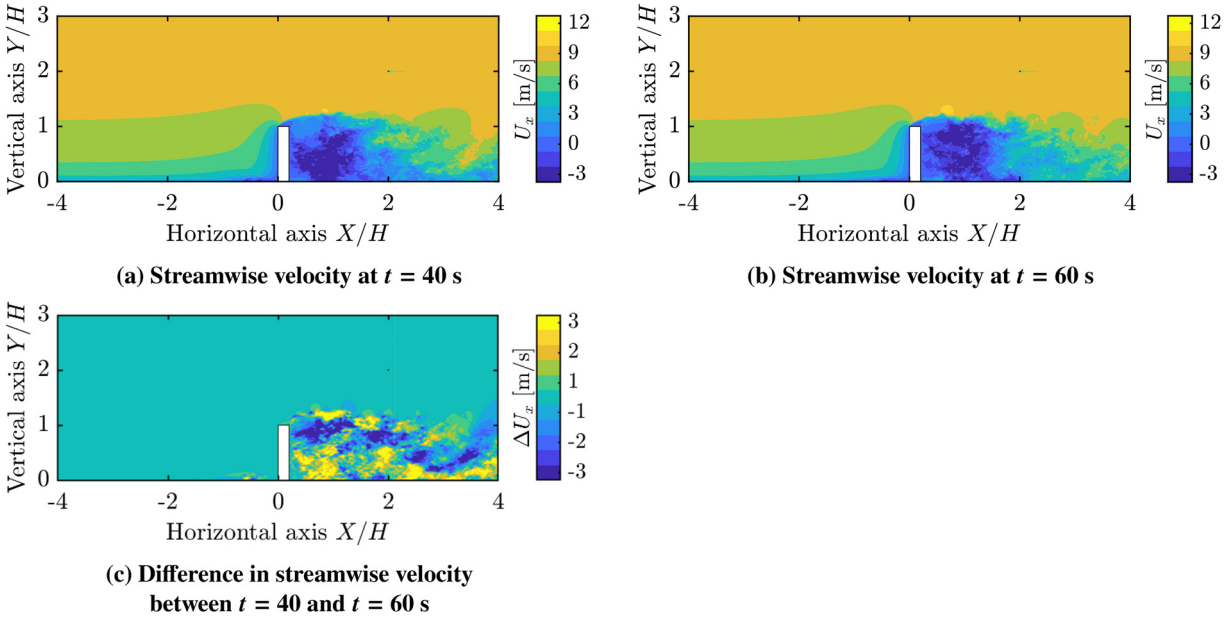

(a) Streamwise velocity at t = 40 s

(b) Streamwise velocity at t = 60 s

(c) Difference in streamwise velocity between t = 40 and t = 60 s

FIG. 5. Instantaneous streamwise velocity at two different time instances at $\mathbf{Z/H} = \mathbf{0}$ (fine simulation).

instances [Figs. 6(d) and 6(e)] show noticeable shifts in interference fringes compared to the no-convection case. These shifts are dependent on the wake evolution and vary between the two time instances due to differences in the instantaneous flowfield (Fig. 5).

The corresponding SPL difference field, shown in Fig. 6(f), highlights regions of significant temporal variation. The localized peaks near the inlet in ΔSPL should therefore be interpreted as indicators of relative sensitivity due to low baseline p_{rms} values rather than absolute increases in acoustic energy. Beyond these regions, prominent variations are observed above and slightly upstream of the building, as well as in the downstream wake. The variability in the downstream wake region is directly attributable to the unsteady wake flow. In contrast, fluctuations above the building result from changes in rays reflected from the building's top edge, modulated by vortex shedding.

Significant differences are also observed in regions perpendicular to the source dipole axis, where the noise level is comparatively lower and, consequently, relative changes in decibel values are amplified. Here, direct acoustic contributions are minimal, and dominant noise arises from rays reflected off the ground that pass through the unsteady wake, making this region sensitive to wake-induced fluctuations. The shadow zone upstream of the building, where only diffracted rays contribute, also exhibits some sensitivity. Temporal variations in the building wake and the upstream horseshoe vortex alter the diffraction at the building edges, resulting in time-varying SPL distributions in this region.

D. Statistical characterization of acoustic variability (fine simulation)

This section quantifies the temporal variability in the acoustic field caused by the unsteady building wake. First, spatial maps of the mean and standard deviation of p_{rms} and the corresponding SPL are presented to quantify acoustic variability over time. This is followed by an analysis that links the observed variability in p_{rms} to low-frequency velocity fluctuations, indicative of turbulent wake structures.

1. Mean and standard deviation of SPL

To characterize the statistical behavior of the acoustic field over time, the 40 s acoustic signal was segmented into 0.2 s segments with 50% overlap, yielding 399 segments and a frequency resolution of 5 Hz. Each segment was bandpass-filtered in the [95, 105] Hz range to isolate the source frequency at 100 Hz.

From these bandpass-filtered signals, the mean and standard deviation of p_{rms} were computed across all segments. The mean SPL is obtained from the time-averaged p_{rms} values using Eq. (3). To quantify temporal variability in the acoustic field, an equivalent standard deviation of SPL is then derived from the fluctuations in p_{rms} as defined in Eq. (4). This definition follows directly from the logarithmic relationship between SPL and p_{rms}, providing a physically consistent measure of temporal acoustic variability,

$$\overline{\mathrm{SPL}} = 20\log_{10}\left(\frac{\overline{p_{\mathrm{rms}}}}{p_{\mathrm{ref}}}\right), \tag{3}$$

$$\begin{aligned}\sigma(\mathrm{SPL}) &= 20\log_{10}\left(\frac{\overline{p_{\mathrm{rms}}} + \sigma(p_{\mathrm{rms}})}{p_{\mathrm{ref}}}\right) \\ &\quad - 20\log_{10}\left(\frac{\overline{p_{\mathrm{rms}}}}{p_{\mathrm{ref}}}\right) \\ &= 20\log_{10}\left(1 + \frac{\sigma(p_{\mathrm{rms}})}{\overline{p_{\mathrm{rms}}}}\right).\end{aligned} \tag{4}$$

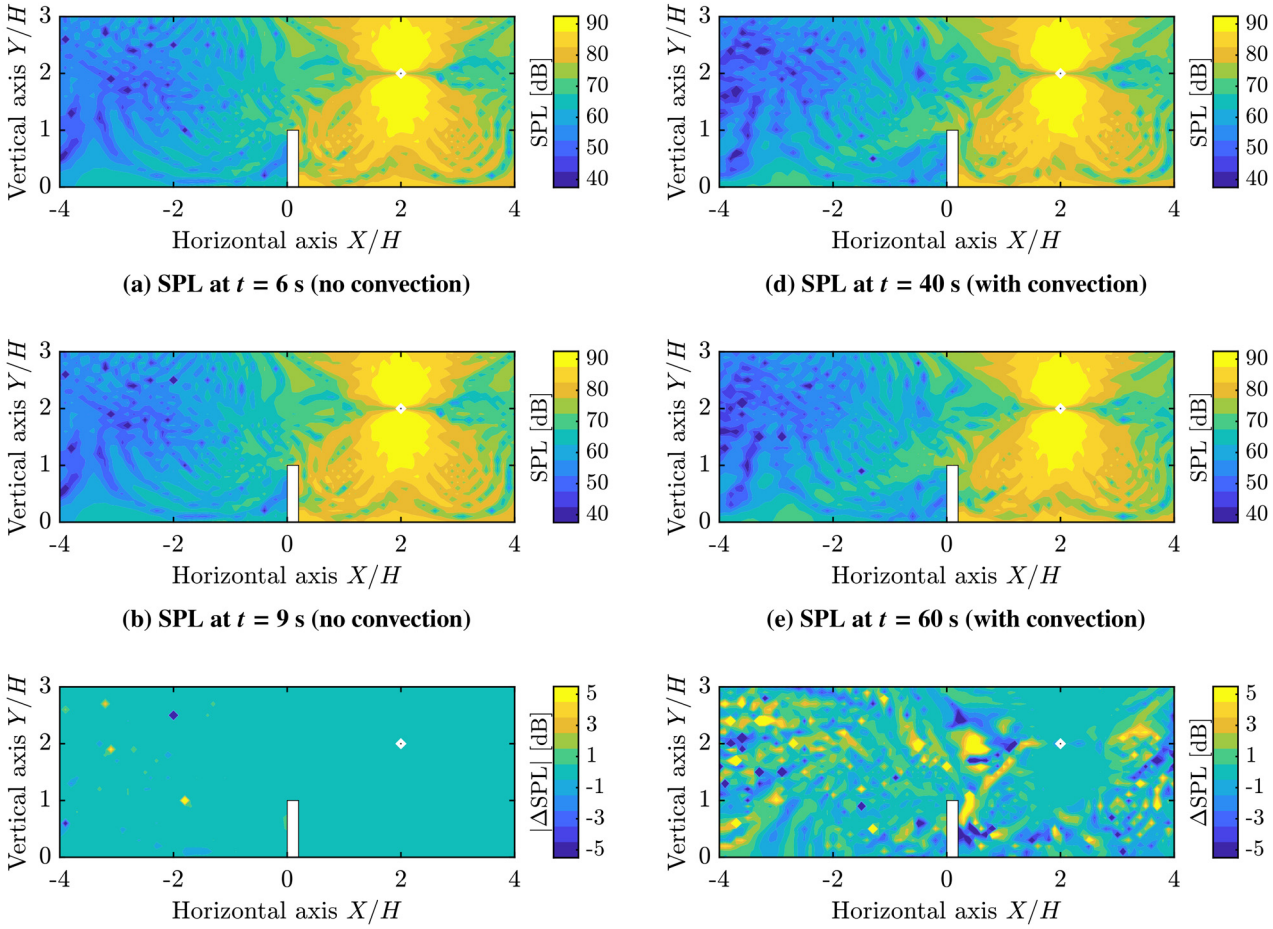

(a) SPL at t = 6 s (no convection)

(d) SPL at t = 40 s (with convection)

(b) SPL at t = 9 s (no convection)

(e) SPL at t = 60 s (with convection)

(c) Difference in SPL between t = 6 and 9 s (no convection)

(f) Difference in SPL between t = 40 and t = 60 s (with convection)

FIG. 6. Instantaneous SPL and differences at selected time instances for $\boldsymbol{f} = [\mathbf{95}\ \mathbf{105}]$ Hz at $\boldsymbol{Z/H} = \mathbf{0}$ (fine simulation).

This formulation highlights that SPL variability is governed by relative pressure fluctuations, $\sigma(p_{\mathrm{rms}})/\overline{p_{\mathrm{rms}}}$, rather than by their absolute magnitude. The spatial distributions of the resulting quantities are shown in Fig. 7.

In the mean pressure field [Fig. 7(a)], the highest $\overline{p_{\mathrm{rms}}}$ values are observed near the dipole source, as expected. Interference patterns arising from reflections off the building and ground create local maxima and minima, particularly in the wake region. The building also casts a clear shadow upstream, where only diffracted rays reach, resulting in reduced $\overline{p_{\mathrm{rms}}}$. The corresponding mean SPL field [Fig. 7(c)] derived from $\overline{p_{\mathrm{rms}}}$ values aligns with these features and confirms earlier observations from Fig. 6.

The influence of wake unsteadiness on p_{rms} is evident in the standard deviation field shown in Fig. 7(b). It should be noted that the unsteady data are available only for a 40 s interval, which may not be sufficient to produce a fully spatially smooth field. However, verification using shorter segments confirmed that the overall trends and spatial distribution of $\sigma(p_{\mathrm{rms}})$ remain consistent. Pressure fluctuations are most pronounced in the downstream wake region, with the strongest absolute fluctuations in the region extending up to approximately $2H$ from the building. As acoustic rays are reflected from the ground and building interact with turbulent structures, a significant variability in p_{rms} is observable well beyond the boundaries of the physical wake [compare to Fig. 2(d)].

When the fluctuations in p_{rms} are translated into SPL variability using Eq. (4), a consistent trend emerges: the largest SPL standard deviations appear in regions that coincide with local minima in the mean SPL field. Since $\sigma(\mathrm{SPL}) \propto \sigma(p_{\mathrm{rms}})/\overline{p_{\mathrm{rms}}}$, such regions are inherently more sensitive, such that even moderate pressure variations result in large decibel fluctuations. Low $\overline{p_{\mathrm{rms}}}$ values may result from: (1) the large distance from the source (e.g., near the inlet), (2) destructive interference between multiple rays of comparable strength passing through an unsteady wake (e.g., within the building wake or above the rooftop), or (3) dominance of an acoustic contribution from a ray traversing a region of significant turbulence (e.g., along the dipole axis). In the presence of an unsteady wake, such rays are continuously perturbed, causing them to arrive at slightly shifted locations or with varying phase differences over time. The resulting superposition yields time-varying p_{rms}, and, due to the low baseline level, these variations manifest as pronounced SPL fluctuations.

https://doi.org/10.1121/10.0042402

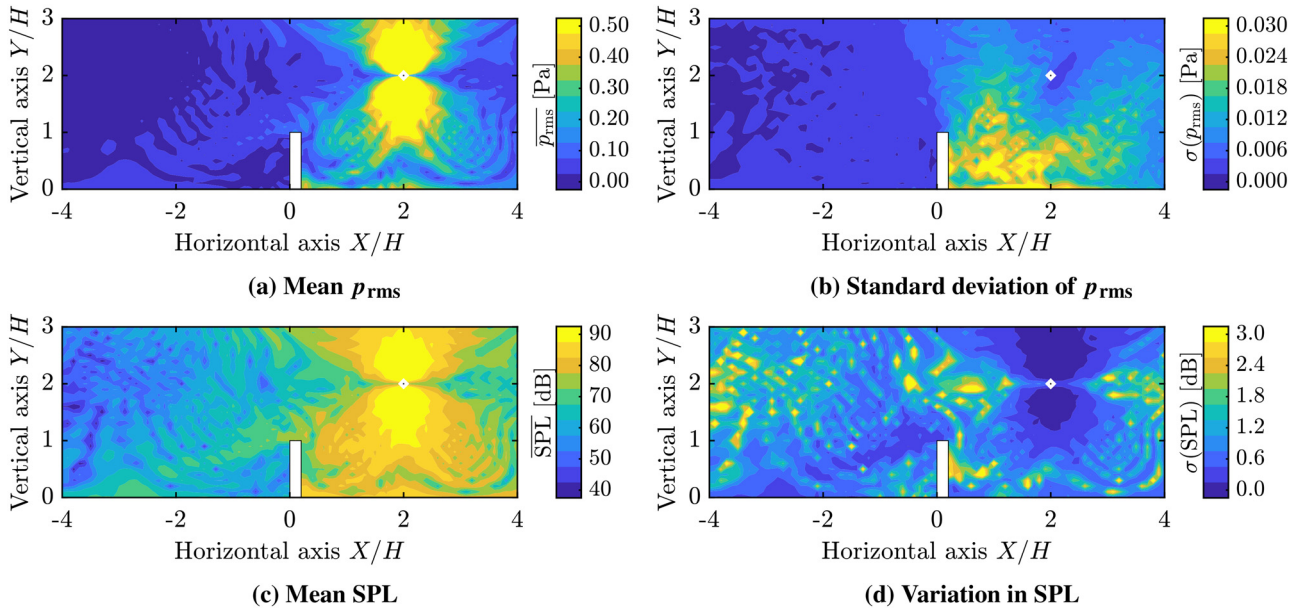

(a) Mean p_{rms} **(b) Standard deviation of p_{rms}**

(c) Mean SPL **(d) Variation in SPL**

FIG. 7. Variability of noise in $\boldsymbol{Z/H = 0}$ plane (fine simulation).

2. Correlation between turbulence and acoustic variability

To investigate the correlation between turbulence encountered along a ray and the resulting acoustic variability, multiple rays of 95 m length were investigated at angles ranging from 90° to 270°, in increments of 5° [see Fig. 8(a)]. Here, "rays" denote straight-line propagation paths from the source through the flowfield, used to relate flow fluctuations encountered along different directions to the observed acoustic variability. Based on expected acoustic reflections from the building, the rays can be categorized into three groups: (1) 90° to 120°, where no reflections from the building are expected, (2) 120° to 180°, where reflections from both the building and the ground are expected, (3) 180° to 270°, where no direct reflections from the building are expected. For ease of interpretation, these regions are overlaid on the contour plot of $\sigma(p_{\text{rms}})$ in Fig. 8(a) [previously shown in Fig. 7(b)]. The first and third regions are shaded with a partially transparent red patch, while the second region is shaded with a partially transparent blue patch.

Along each ray, the acoustic variability, denoted by $\bar{\sigma}_{p,\text{norm}}$ [see Eq. (5)], is quantified by the normalized, spatially averaged standard deviation of the RMS acoustic pressure along the ray. At each point along the ray, the local fluctuation $\sigma(p_{\text{rms}})(l)$ is normalized by the expected RMS pressure at distance l from the source, approximated via spherical spreading as $p_{\text{rms,source}}/l$, where $p_{\text{rms,source}} = 17.30$ Pa is the average RMS pressure over a 1 m radius sphere surrounding the source. Similarly, the velocity fluctuation metric $\bar{\sigma}_{|\vec{U}|,\text{norm}}$ [see Eq. (6)], is defined as the spatially averaged standard deviation of the velocity magnitude, normalized by the maximum standard deviation observed in the wake, $\sigma(|\vec{U}|)_{\max} = 2.38$ m/s.

To isolate the relevant physical phenomena, p_{rms} was bandpass-filtered between 95 and 105 Hz to capture the acoustic source frequency, while the velocity magnitude $|\vec{U}|$

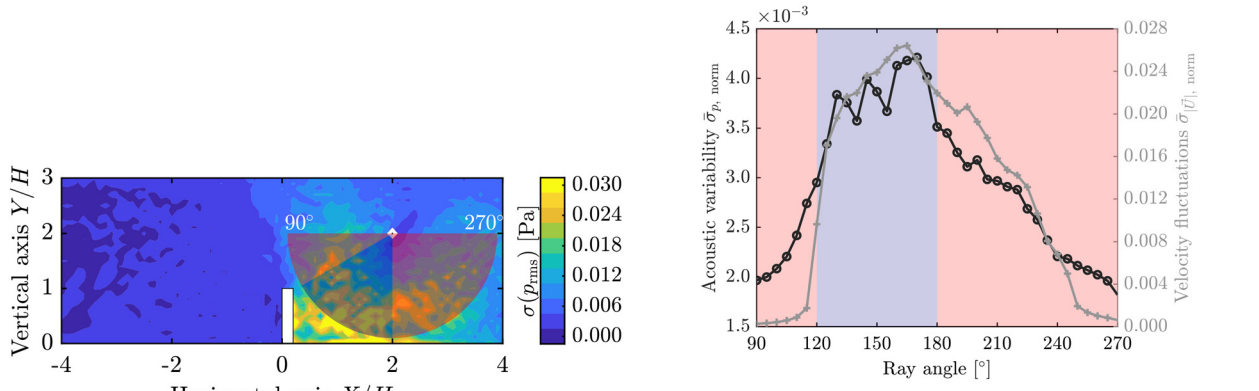

(a) Rays plotted over σ (p_{rms}) contours **(b) Normalized acoustic variability and velocity fluctuations as a function of ray angle**

FIG. 8. Correlation between turbulence-induced velocity fluctuations and acoustic variability along rays.

was low-pass filtered up to 10 Hz to isolate turbulence-induced fluctuations,

$$\bar{\sigma}_{p,\mathrm{norm}} = \sqrt{\frac{1}{L}\int_0^L \left(\frac{\sigma(p_{\mathrm{rms}})(l)\cdot l}{p_{\mathrm{rms,\,source}}}\right)^2 dl}, \tag{5}$$

$$\bar{\sigma}_{|\vec{U}|,\mathrm{norm}} = \sqrt{\frac{1}{L}\int_0^L \left(\frac{\sigma\left(|\vec{U}|\right)(l)}{\sigma\left(|\vec{U}|\right)_{\max}}\right)^2 dl}. \tag{6}$$

Figure 8(b) shows the acoustic variability and velocity fluctuations for different rays. In the first and third regions, a direct correlation is observed between acoustic variability and velocity fluctuations. In the first region (90°–120°), both quantities increase monotonically as the rays penetrate deeper into the building wake. The $\bar{\sigma}_{p,\mathrm{norm}}$ increases from 2.0×10^{-3} at 90° to 3.0×10^{-3} at 120°, while $\bar{\sigma}_{|\vec{U}|,\mathrm{norm}}$ increases from 0.0003 to 0.0096.

In the third region (180°–270°), the rays progressively graze the wake at shallower angles. Accordingly, both $\bar{\sigma}_{p,\mathrm{norm}}$ and $\bar{\sigma}_{|\vec{U}|,\mathrm{norm}}$ decrease nearly monotonically. The $\bar{\sigma}_{p,\mathrm{norm}}$ drops from 3.5×10^{-3} to 1.8×10^{-3}, while $\bar{\sigma}_{|\vec{U}|,\mathrm{norm}}$ decreases from 0.0220 to 0.0006.

In contrast, the second region (120°–180°) does not exhibit a clear correlation between $\bar{\sigma}_{p,\mathrm{norm}}$ and $\bar{\sigma}_{|\vec{U}|,\mathrm{norm}}$. The velocity fluctuation metric $\bar{\sigma}_{|\vec{U}|,\mathrm{norm}}$ increases monotonically up to a peak at 165° before decreasing monotonically thereafter. In comparison, while $\bar{\sigma}_{p,\mathrm{norm}}$ displays a broadly similar overall trend, it features local maxima and minima throughout this region. These local fluctuations, absent in the velocity field, are attributed to strong acoustic reflections from the ground and the building, which cause constructive and destructive interference effects.

These results indicate that turbulence-induced velocity fluctuations along the direct ray are the dominant contributor to acoustic variability in regions with minimal reflections. In reflection-dominated zones, however, acoustic variability is also affected by additional mechanisms, such as interference between multiple rays and phase shifts. It should be noted that the current analysis considers only a single configuration; additional simulations with different source positions, heights, frequencies, and wind profiles are necessary to verify the generality of these trends and provide a first quantitative assessment of the observed variability.

IV. CONCLUDING REMARKS

This paper investigated the influence of turbulence induced by a building on the noise footprint of a simplified acoustic dipole using time-resolved LB-VLES simulations. The acoustic source, modeled as a vertically oscillating cube at 100 Hz, was placed downstream of a mid-rise building representative of compact urban structures.

The results show that the unsteady wake generated by the building induces temporal shifts in interference fringes within the noise footprint. As the SPL variability scales approximately with $\sigma(p_{\mathrm{rms}})/\overline{p_{\mathrm{rms}}}$, the largest SPL fluctuations, reaching and locally exceeding 3 dB, are observed in regions where these fringe shifts occur, indicating a substantial relative change in p_{rms} at these locations. Acoustic variations of several decibels are well above typical just-noticeable differences and are therefore expected to be clearly perceptible, potentially leading to increased annoyance. The magnitude of this building-induced variability is comparable to SPL fluctuations commonly attributed to atmospheric turbulence in outdoor propagation studies, suggesting that wake-generated unsteadiness from nearby structures may represent an additional source of perceptible acoustic variability that is not currently accounted for in standard noise modeling and certification frameworks.

Analysis of bandpass-filtered pressure fluctuations further demonstrates that turbulence-induced acoustic variability is not confined to the physical extent of the wake. Instead, zones of elevated variability extend beyond the wake due to acoustic reflections from the building and the ground, implying that wake geometry alone is insufficient to identify regions of increased acoustic modulation. This observation motivates the use of efficient reduced-order approaches that exploit the strong time scale separation between turbulence and acoustics, such as frozen-flow–based noise propagation methods coupled with ray tracing. While promising, the accuracy and applicability of such approaches require further investigation.

Directional analysis revealed a strong correlation between fluctuations in low-frequency velocity magnitude and high-frequency acoustic variability along direct propagation paths in regions with limited reflections. In contrast, in regions dominated by strong reflections, acoustic variability is influenced by contributions from indirect paths, and correlations based solely on direct rays become insufficient. This highlights the importance of accounting for reflective propagation mechanisms when analyzing turbulence-induced noise-variability in urban environments.

Finally, it is worth noting that the present conclusions are based on a single configuration with a simplified source representation. Additional simulations covering different source locations, heights, frequencies, and wind profiles would be required to assess the generality of the observed trends. Nevertheless, the present results underscore the importance of accounting for building-induced turbulence when predicting AAM noise footprints in urban settings, both for accurate noise modeling and for the design of future experimental and operational strategies.

ACKNOWLEDGMENTS

The research leading to these results is part of the eVTOLUTION project. This project has received funding from the European Union's Horizon Europe programme under Grant No. 101138209. This work made use of the Dutch national e-infrastructure with the support of the SURF Cooperative using Grant No. EINF-9226.

https://doi.org/10.1121/10.0042402

AUTHOR DECLARATIONS

Conflict of Interest

The authors have no conflicts to disclose.

DATA AVAILABILITY

The data that support the findings of this study are available from the corresponding author upon reasonable request.

[1]T. C. Stokkermans, D. Usai, T. Sinnige, and L. L. Veldhuis, "Aerodynamic interaction effects between propellers in typical evtol vehicle configurations," J. Aircraft **58**(4), 815–833 (2021).

[2]NASA, "Urban air mobility (UAM) market study," https://ntrs.nasa.gov/api/citations/20190002046/downloads/20190002046.pdf (Last viewed May 22, 2025).

[3]European Union Aviation Safety Agency, *Prototype Technical Specifications for the Design of VFR Vertiports for Operation with Manned VTOL-Capable Aircraft Certified in the Enhanced Category (PTS-VPT-DSN)* (European Union Aviation Safety Agency, Cologne, Germany, 2022).

[4]European Union Aviation Safety Agency, *Study on the Societal Acceptance of Urban Air Mobility in Europe* (European Union Aviation Safety Agency, Cologne, Germany, 2021).

[5]S. A. Rizzi, D. L. Huff, D. D. Boyd, P. Bent, B. S. Henderson, K. A. Pascioni, D. C. Sargent, D. L. Josephson, M. Marsan, H. B. He, and R. Sinder, "Urban air mobility noise: Current practice, gaps, and recommendations," NASA/ TP-20205007433, NASA, Washington, DC (2020).

[6]L. Babetto, A. Kirste, J. Deng, M. Husemann, and E. Stumpf, "Adoption of the urban air mobility system: Analysis of technical, legal and social aspects from a European perspective," J. Air Transp. Res. Soc. **1**(1), 152–174 (2023).

[7]C. E. Tinney and J. Sirohi, "Multirotor drone noise at static thrust," AIAA J. **56**(7), 2816–2826 (2018).

[8]H. Lee and D.-J. Lee, "Rotor interactional effects on aerodynamic and noise characteristics of a small multirotor unmanned aerial vehicle," Phys. Fluids **32**(4), 047107 (2020).

[9]R. S. McKay, M. J. Kingan, S. T. Go, and R. Jung, "Experimental and analytical investigation of contra-rotating multi-rotor UAV propeller noise," Appl. Acoust. **177**, 107850 (2021).

[10]R. H. Lyon, "Reverberation for multipath propagation in urban areas," J. Acoust. Soc. Am. **53**(S1), 339–340 (1973).

[11]V. E. Ostashev and D. K. Wilson, *Acoustics in Moving Inhomogeneous Media*, 2nd ed. (CRC Press/Taylor & Francis, Boca Raton, FL, 2015).

[12]S. Cheinet, M. Cosnefroy, F. Königstein, W. Rickert, M. Christoph, S. L. Collier, A. Dagallier, L. Ehrhardt, V. E. Ostashev, A. Stefanovic, T. Wessling, and D. K. Wilson, "An experimental study of the atmospheric-driven variability of impulse sounds," J. Acoust. Soc. Am. **144**(2), 822–840 (2018).

[13]F. Yunus, D. Casalino, F. Avallone, and D. Ragni, "Toward inclusion of atmospheric effects in the aircraft community noise predictions," J. Acoust. Soc. Am. **150**(2), 759–768 (2021).

[14]R. E. Britter and S. R. Hanna, "Flow and dispersion in urban areas," Annu. Rev. Fluid Mech. **35**, 469–496 (2003).

[15]H. Fernando, "Fluid dynamics of urban atmospheres in complex terrain," Annu. Rev. Fluid Mech. **42**, 365–389 (2010).

[16]Y. Tominaga and T. Stathopoulos, "CFD simulation of near-field pollutant dispersion in the urban environment: A review of current modeling techniques," Atmos. Environ. **79**, 716–730 (2013).

[17]D. Perry, "Blade release due to manufacturing defect doomed VX4 prototype, says UK AAIB," https://www.flightglobal.com/aerospace/blade-release-due-to-manufacturing-defect-doomed-vx4-prototype-says-uk-aaib/158122.article (Last viewed May 22, 2025).

[18]O. Johnson, "Cityairbus set for first flight in march," https://verticalmag.com/news/cityairbus-set-for-first-flight-in-march/ (Last viewed May 22, 2025).

[19]G. Warwick, "Nasa's electric-propulsion wing test helps shape next X-plane," https://aviationweek.com/aerospace/nasas-electric-propulsion-wing-test-helps-shape-next-x-plane (Last viewed May 22, 2025).

[20]K. A. Pascioni, M. E. Watts, M. Houston, A. Lind, J. H. Stephenson, and J. Bain, "Acoustic flight test of the Joby Aviation advanced air mobility prototype vehicle," in *28th AIAA/CEAS Aeroacoustics 2022 Conference* (American Institute of Aeronautics and Astronautics, Reston, VA, 2022), p. 3036.

[21]A. Thai and A. S. Engineer, "Flyover noise computations of the Joby Aviation aircraft," Horizon **270**(300), 60 (2023), available at https://legacy.vtol.org/store/product/flyover-noise-computations-of-the-joby-aviation-aircraft-17959.cfm.

[22]K. A. Pascioni, A. D. Thai, and J. J. Bain, "Propeller source noise separation from flight test measurements of the Joby Aviation aircraft," in *30th AIAA/CEAS Aeroacoustics Conference (2024)* (American Institute of Aeronautics and Astronautics, Reston, VA, 2024), p. 3231.

[23]E. Grande, S. Shubham, F. Avallone, D. Ragni, and D. Casalino, "Computational aeroacoustic study of co-rotating rotors in hover," Aerosp. Sci. Technol. **153**, 109381 (2024).

[24]D. Casalino, G. Romani, L. M. Pii, and R. Colombo, "Flow confinement effects on sUAS rotor noise," Aerosp. Sci. Technol. **143**, 108756 (2023).

[25]D. Casalino, G. Romani, R. Zhang, and H. Chen, "Lattice-Boltzmann calculations of rotor aeroacoustics in transitional boundary layer regime," Aerosp. Sci. Technol. **130**, 107953 (2022).

[26]G. Romani, E. Grande, F. Avallone, D. Ragni, and D. Casalino, "Computational study of flow incidence effects on the aeroacoustics of low blade-tip Mach number propellers," Aerosp. Sci. Technol. **120**, 107275 (2022).

[27]G. Romani, E. Grande, F. Avallone, D. Ragni, and D. Casalino, "Performance and noise prediction of low-Reynolds number propellers using the Lattice-Boltzmann method," Aerosp. Sci. Technol. **125**, 107086 (2022).

[28]D. Casalino, W. C. van der Velden, G. Romani, and I. Gonzalez-Martino, "Aeroacoustic analysis of urban air operations using the LB/VLES method," in *25th AIAA/CEAS Aeroacoustics Conference* (American Institute of Aeronautics and Astronautics, Reston, VA, 2019), p. 2662.

[29]D. Casalino, W. C. van der Velden, and G. Romani, "Community noise of urban air transportation vehicles," in *AIAA Scitech 2019 Forum* (American Institute of Aeronautics and Astronautics, Reston, VA, 2019), p. 1834.

[30]G. Bres, F. Pérot, and D. Freed, "Properties of the lattice boltzmann method for acoustics," in *15th AIAA/CEAS Aeroacoustics Conference (30th AIAA Aeroacoustics Conference)* (American Institute of Aeronautics and Astronautics, Reston, VA, 2009), p. 3395.

[31]S. Marié, D. Ricot, and P. Sagaut, "Comparison between lattice Boltzmann method and Navier–Stokes high order schemes for computational aeroacoustics," J. Comput. Phys. **228**(4), 1056–1070 (2009).

[32]V. Yakhot and S. A. Orszag, "Renormalization group analysis of turbulence. I. Basic theory," J. Sci. Comput. **1**(1), 3–51 (1986).

[33]H. Chen, S. A. Orszag, I. Staroselsky, and S. Succi, "Expanded analogy between Boltzmann kinetic theory of fluids and turbulence," J. Fluid Mech. **519**, 301–314 (2004).

[34]S. Succi, *The Lattice Boltzmann Equation: For Fluid Dynamics and Beyond* (Oxford University Press, Oxford, UK, 2001).

[35]X. Shan, X.-F. Yuan, and H. Chen, "Kinetic theory representation of hydrodynamics: A way beyond the Navier–Stokes equation," J. Fluid Mech. **550**, 413–441 (2006).

[36]K. Al-Kodmany, *The Vertical City: A Sustainable Development Model* (WIT Press, Southampton, UK, 2018).

[37]V. Cheng, "Understanding density and high density," in *Designing High-Density Cities for Social and Environmental Sustainability*, edited by E. Ng (Earthscan, London, UK, 2010), pp. 3–17.

[38]E. Salomons, *Computational Atmospheric Acoustics* (Kluwer Academic, Dordrecht, The Netherlands, 2001), pp. 40–42.

[39]C. M. Teixeira, "Incorporating turbulence models into the Lattice-Boltzmann method," Int. J. Mod. Phys. C **09**(08), 1159–1175 (1998).

[40]D. C. Wilcox, *Turbulence Modelling for CFD*, 3rd ed. (DCW Industries, La Canada, CA, 2006).

[41]B. E. Launder and D. B. Spalding, "The numerical computation of turbulent flows," in *Numerical Prediction of Flow, Heat Transfer, Turbulence and Combustion* (Elsevier, Amsterdam, The Netherlands, 1983), pp. 96–116.

[42]Y. Nakamura, "Vortex shedding from bluff bodies and a universal Strouhal number," J. Fluids Struct. **10**(2), 159–171 (1996).

[43]T. Okaze, H. Kikumoto, H. Ono, M. Imano, N. Ikegaya, T. Hasama, K. Nakao, T. Kishida, Y. Tabata, K. Nakajima, R. Yoshie, and Y. Tominaga, "Large-eddy simulation of flow around an isolated building: A step-by-step analysis of influencing factors on turbulent statistics," Build. Environ. **202**, 108021 (2021).

[44]P. Ding, X. Zhou, H. Wu, and Q. Chen, "An efficient numerical approach for simulating airflows around an isolated building," Build. Environ. **210**, 108709 (2022).

[45]S. B. Pope, "Turbulent flows," Meas. Sci. Technol. **12**(11), 182–191 (2001).

[46]J. Jeong and F. Hussain, "On the identification of a vortex," J. Fluid Mech. **285**, 69–94 (1995).